Nano Research
2022, 15(12): 10185–10193

ISSN 1998-0124 CN 11-5974/O4
https://doi.org/10.1007/s12274-022-4681-z

Research Article

Porous copper cluster-based MOF with strong cuprophilic interactions for highly selective electrocatalytic reduction of CO_2 to CH_4

Long-Zhang Dong[1,2,§], Yun-Feng Lu[2,§], Rui Wang[2], Jie Zhou[1], Yu Zhang[2], Lei Zhang[1], Jiang Liu[1,2], Shun-Li Li[1,2], and Ya-Qian Lan[1,2] (✉)

[1] *National and Local Joint Engineering Research Center of MPTES in High Energy and Safety LIBs, Engineering Research Center of MTEES (Ministry of Education), Key Lab. of ETESPG (GHEI), School of Chemistry, South China Normal University, Guangzhou 510006, China*

[2] *Jiangsu Collaborative Innovation Centre of Biomedical Functional Materials, Jiangsu Key Laboratory of New Power Batteries, School of Chemistry and Materials Science, Nanjing Normal University, Nanjing 210023, China*

[§] *Long-Zhang Dong and Yun-Feng Lu contributed equally to this work.*

Received: 9 May 2022 / **Revised:** 4 June 2022 / **Accepted:** 20 June 2022

ABSTRACT

It is well known that the low-valent Cu species are important catalytically active centers in the reduction of CO_2 to hydrocarbon products. However, the Cu(I)-based catalysts are easily reduced during the electroreduction of CO_2, which causes phase transformation of catalysts and leads to a decrease of intrinsic catalytic activity. Therefore, it is of great significance to synthesize Cu(I)-based catalysts with specific interactions that can keep the catalytically active Cu sites stable in the electrocatalytic process. Based on the above considerations, a hexanuclear Cu cluster with strong cuprophilic interactions has been designed and utilized as a secondary building unit (SBU) to construct a stable metal-organic framework (MOF) electrocatalyst (**NNU-50**). As expected, the **NNU-50** has served as an effective electrocatalyst for the CO_2-to-CH_4 conversion by exhibiting a high Faradaic efficiency for CH_4 (FE_{CH_4}) of 66.40% and a large current density of ~ 400 mA·cm^{-2} at −1.0 V vs. reversible hydrogen electrode (RHE), which is one of the best catalytic performances among the stable MOF electrocatalysts until now. This work contributes more ideas for the design of stable and efficient MOF-based electrocatalysts for CO_2 reduction reaction.

KEYWORDS

metal-organic framework, cuprophilic interactions, carbon dioxide, electroreduction

1 Introduction

The transformation of CO_2 into energy substances (e.g., CO, HCOOH, CH_4, C_2H_4, and alcohols) by electrochemical methods is important to achieve carbon neutrality [1–5]. Among the CO_2 electroreduction products, CH_4 is favored for its high energy density, broader industrial applications, and potential to become a new alternative to fossil fuels [3, 6]. However, the formation of high value-added products involves a complex multiple H^+/e^- process, which causes the poor selectivity of CO_2-to-CH_4 electroreduction is still not sufficient for practical industrial production [7–9]. Therefore, the construction of novel and efficient electrocatalysts for the CO_2-to-CH_4 reaction is a particularly important but challenging work. At present, Cu-based materials (Cu oxides [10, 11], Cu nanoparticles [12, 13], Cu-based complexes [14–18], etc.) have been generally accepted as effective electrocatalysts for the reduction of CO_2 to high value-added products. According to previous reports, the low-valent Cu species in electrocatalytic CO_2 reduction (ECR) may facilitate the formation of high value-added products [19–24]. Therefore, the stabilization of Cu(I) active sites in electrocatalysts will have a meaningful impact on ECR to specific products [25]. Taking the above factors into account, the designing of Cu(I)-based catalysts with strongly cuprophilic interactions to stabilize Cu(I) ions is a promising strategy to achieve efficient and selective electroconversion of CO_2 [26].

Metal-organic framework (MOF) is crystalline porous materials formed by the self-assembly of organic ligands and metal ions or clusters [27]. MOF has wide application prospects in catalysis due to its well-defined structural information and high designability [27, 28]. The unique designable advantages can facilitate the introduction of cuprophilic interactions into the secondary building units (SBU) of the MOF structures. Moreover, the permanent porosity in MOF can provide more catalytic sites and make it more convenient for CO_2 to adsorb and react, which will make the reaction speed faster [29]. Besides, the well-defined structure of MOF helps to establish an intuitive understanding of the effect of cuprophilic interactions on ECR performance [15, 23, 24, 30–35]. More importantly, the atomic-level accurate catalyst models constructed by MOF materials are conducive to building clear conformational relationships to further investigate the mechanism for hydrocarbon generation from ECR and provide insights for designing more efficient electrocatalysts.

Herein, a cluster-based MOF ($Cu_3(Me_4BPz)_{3/2}$, **NNU-50**;

Address correspondence to yqlan@njnu.edu.cn, yqlan@m.scnu.edu.cn

Me_4BPz = 3,3',5,5'-tetramethyl-4,4'-bipyrazolyl) has been designed and synthesized as an electrocatalyst for ECR in the gas diffusion flow cell using bipyrazole ligands and Cu(I) ions. The existence of strong cuprophilic interactions in the hexanuclear Cu cluster node makes it possible for **NNU-50** to stabilize the Cu(I) sites during the process of ECR and thus realize the electrochemical conversion of CO_2 to high valued products. Furthermore, there are abundant pores in **NNU-50**, allowing the efficient enrichment and adsorption of CO_2 on the catalytically active sites. As expected, the ECR test results show **NNU-50** possesses excellent electrocatalytic performance for the CO_2-to-CH_4 conversion. Specifically, the **NNU-50** delivers an excellent Faradaic efficiency (FE) for CH_4 (FE_{CH_4}) of 66.40% at −1.0 V vs. reversible hydrogen electrode (RHE) with a large current density of 398.02 mA·cm^{-2}, which is one of the best catalytic performances among the stable MOF electrocatalysts to date. It is worthy to note that the FE_{CH_4} can keep higher than 58% from −0.9 to −1.2 V vs. RHE and the selectivity for hydrocarbon ($FE_{hydrocarbon}$) is up to 81.50% at −1.0 V vs. RHE, which further indicates the excellent performance of **NNU-50**. Moreover, the key intermediates involved in the CH_4 formation pathway (such as $*CH_2O$ and $*OCH_3$) have been detected by *in situ* diffuse reflectance infrared Fourier transform spectroscopy (DRIFTS) and the possible electrocatalytic reaction mechanism for ECR-to-CH_4 conversion has been speculated based on the intermediates. At the same time, a metal-organic complex **Cu_6MePz**, whose structure is similar to the SBU of **NNU-50**, was also synthesized to be an ECR catalyst. By comparing the ECR test results of **NNU-50** and **Cu_6MePz**, the effect of pore structure of MOF on the catalytic performance was explored. This work will help shed light on the mechanism for CO_2-to-CH_4 electroconversion and provide inspiration for the design of more effective electrocatalysts applying to the process.

2 Experimental

2.1 Synthesis of 1,1,2,2-tetraacetylethane

1,1,2,2-Tetraacetylethane was prepared following the modified reported method [36]. At first, 0.1 mol acetylacetone was added dropwise to 600 mL aqueous solution containing 0.21 mol $(NH_3)_2Ce(NO_3)_6$ at 5 °C controlled by an ice water bath with continuous sonicating and manual stirring until the red color faded. Subsequently, the mixture was stood for 4 h before being filtered and washed with water to obtain the product.

2.2 Synthesis of Me_4BPz

Me_4BPz was synthesized by the modified reported method [37]. 9.92 g (50 mmol) of 1,1,2,2-tetraacetyl ethane was dispersed in 20 mL of water and 25 mL (~ 250 mmol) 50 wt.% hydrazine hydrate was added rapidly at −20 °C with mechanical stirring. Afterward, the mechanical stirring would continue at room temperature for another 2 h. Then the mixture was filtered and washed with water. The compound could be purified by recrystallization from methanol and water. Finally, the colorless crystals were obtained.

2.3 Synthesis of NNU-50

1 mmol $Cu(ClO_4)_2·6H_2O$ and 0.2 mmol Me_4BPz were ultrasonically dissolved in 4 mL N,N-dimethylformamide (DMF), and transferred to 10 mL glass vials. After adding 32 μL HCl, the vial was sealed. Then the mixed solution was heated to 100 °C for 8 h. Finally, the mixture was filtered while hot and washed with DMF and methanol to obtain slightly yellow block crystals.

2.4 Synthesis of Cu_6MePz

The **Cu_6MePz** was synthesized using an improved reported method [38]. 0.1 mmol 3,5-dimethylpyrazole and 0.4 mmol $CuCl_2·2H_2O$ were dissolved in 3 mL DMF and 1 mL water, respectively. Then the two solutions were mixed in a 10 mL glass vial and sealed, and the mixed solution was heated to 120 °C for 48 h. Finally, the mixture was filtered while hot and washed with DMF and methanol to obtain colorless block crystals.

2.5 Single-crystal X-ray diffraction (SC-XRD) measurement method

Small amounts of crystals were taken from glass vials, and a clean, regular-shaped crystal was selected and placed in Paratone oil to remove surface adherence under a microscope. Subsequently, this crystal was picked from oil by using Hampton cryoloop, and then the crystal data was collected at 296 K. Bruker APEX Duo II SC-XRD equipped with a CCD area detector was used for indexing and data collection (Mo Kα λ = 0.71073 Å, 30 kV, and 50 mA). The data were integrated and corrected for Lorentz and polarization effects using the SAINT [39] program. Absorption correction was performed using the multi-scan method through the SADABS [39] program. The initial structure was solved by intrinsic phasing method of ShelXT [40] program and refined by using the least squares method of the ShelXL-2018 [41] program in Olex2 [42] software. All non-hydrogen atoms were refined with anisotropic displacement parameters. The electron density contributions of all highly disordered solvent molecules were treated with the SQUEEZE method in PLATON program [43]. The topological analysis of the crystal structure was carried out using the ToposPro [44] program. All single crystal data were available free of charge from the Cambridge Crystallographic Data Center (CCDC) (CCDC number: 2170003).

2.6 Electrochemical experiment measurement method

10 mg electrocatalyst was ground into powder and dispersed in a mixed solution of water (500 μL), ethanol (450 μL), and Nafion D-250 dispersion (50 μL). Then the mixture was sonicated for at least 30 min to form a homogeneous ink. 25 μL of the ink was pipetted and applied uniformly on the gas diffusion layer (GDL) of commercial carbon paper (the coating size was controlled to be 0.25 cm × 1 cm) to form a working electrode.

The ECR reaction tests were carried out in a GDL flow cell with a three-electrode system. The effective area of the working electrode was 0.25 cm^2, and the distance from the working electrode to the anion exchange membrane (Fumasep, FAA3PK130) was about 1.5 mm. The Ag/AgCl electrode with saturated KCl and Pt electrode were used as the reference and counter electrode, respectively. All potentials were converted to the values versus RHE according to the following equation

$$E\,(\text{vs. RHE}) = E\,(\text{vs. Ag/AgCl}) + 0.197\ \text{V} + 0.0591\ \text{V} \times \text{pH}$$

The schematic diagram of the electrochemical device is shown in Fig. S1 in the Electronic Supplementary Material (ESM). The electrolyte (1.0 M KOH) was pumped into the anode and cathode chambers via a peristaltic pump (LongerPump, BT1002J) at 5 mL·min^{-1}. High purity CO_2 (99.999%) passed through the GDL of the cathode chamber at a flow rate of 20 sccm, which was controlled by a mass flow controller (AITOLY, MFC300). The gas outlet of the cathode chamber was connected directly to the 6-port valve of the on-line gas chromatography.

The FEs were calculated using the following equation

$$\text{FE}\% = (nFxV)/j_{\text{Tot}} \times 100$$

n = number of transferred electrons

F = Faraday's constant
x = mole fraction of product
V = total molar flow rate of gas
j_{Tot} = total current density

All ECR experiments were performed on an SP-150 electrochemical workstation (Bio-Logic). Linear sweep voltammetry (LSV) curves were measured in 1 M KOH solution under CO_2/Ar atmosphere to select the appropriate test potential range of the catalyst. The scan range was from 0 to −1.3 V vs. RHE at a rate of 5 mV·s^{-1}. The ECR and LSV experiments were conducted with 90% *iR* compensation at ambient pressure and room temperature. Cyclic voltammetry (CV) tests were performed in 1 M KOH solution at different scan rates without *iR* compensation. Electrochemical impedance spectroscopy (EIS) was tested at −1.0 V vs. RHE over the frequency range: 1 MHz to 0.1 Hz with 10 mV amplitude.

2.7 The analysis of ECR products

The gaseous products (H_2, CO, CH_4, C_2H_4, etc.) were analyzed by an on-line GC (Agilent, 7820A) equipped with dual 6-port valves, flame ionization detector (FID), and thermal conductivity detector (TCD). The gas flow path and chromatographic conditions of GC are shown in Fig. S2 and Table S1 in the ESM. The GC was corrected by the purchased standard gases. The concentrations of the standard mixed gases, chromatograms of FID and TCD, and standard curves of GC have been shown in Table S2, and Figs. S3 and S4 in the ESM, respectively. The gaseous products were quantified by GC after the electrolysis reaction ran at least 200 s. The liquid products were detected by Bruker Avance 400 M nuclear magnetic resonance (NMR) spectrometer.

2.8 Isotope labeling experiments

Isotope labeling experiments were performed using $^{13}CO_2$ instead of $^{12}CO_2$ substrate under identical reaction conditions. And the isotopic analysis of reaction products was conducted by using a 7890B-5977B (Agilent) gas chromatograph-mass spectrometer (GC-MS) equipped with a GS-CarbonPlot (Agilent) capillary column.

2.9 Material characterization

Powder X-ray diffraction (PXRD) data were obtained on Rigaku SmartLab equipped with a Cu Kα radiation source (λ = 1.54060 Å). Scanning electron microscopy (SEM) measurements were conducted on JSM-7600F device with an accelerating voltage of 10 kV. Fourier-transform infrared (FTIR) and attenuated total reflection FTIR (ATR-FTIR) data were collected with a Bruker Alpha II FTIR spectrometer. The *in situ* DRIFTS tests were operated on Thermo Scientific Nicolet-iS50 equipped with mercury cadmium telluride (MCT)/A detector. N_2 and CO_2 adsorption–desorption isotherms were recorded by Quantachrome Instruments Autosorb iQ2. The thermogravimetric analysis (TGA) was carried out using a Diamond DSC Pyris analyzer (Perkin-Elmer) with the following test conditions: from room temperature to 800 °C under nitrogen atmosphere and a heating rate of 10 °C·min^{-1}. Raman spectroscopy was performed on LabRam HR Evolution.

3 Results and discussion

3.1 Crystal structure characterization of NNU-50

The SC-XRD analysis indicated that **NNU-50** belongs to the $I4_1/acd$ space group of the tetragonal crystal system, and the corresponding crystallographic data are shown in Tables S3–S5 in the ESM. There are one and a half Me_4BPz ligands and three crystallographically independent Cu ions in the asymmetric unit, forming a classical triangular trinuclear Cu cluster (Fig. S5 in the ESM). Each Cu ion is coordinated with two nitrogen atoms from different Me_4BPz ligands and forms a linear coordination (Fig. S6 in the ESM). Interestingly, the trinuclear cluster is in the dimeric form in the crystal structure, and there is a strong cuprophilic interaction between the Cu1 atom and Cu3 atom from another adjacent trinuclear cluster (Cu–Cu distance 2.887 Å, Fig. 1(a)). Considering the cuprophilic interaction in the dimer, the nodes can be regarded as a trigonal antiprismatic shaped hexanuclear Cu cluster (Fig. 1(b)). Based on the above analyses, the crystal structure can be described as one ligand linking to two hexanuclear clusters, while each hexanuclear cluster links to six Me_4BPz ligands, thus forming a 6-c net three-dimensional (3D) framework. Subsequently, the crystal structure of **NNU-50** was simplified through ToposPro [44] software as bcs topology type, and the corresponding Schläfli symbol is {4^6.6^9} (Fig. 1(b) and Fig. S7 in the ESM). The tiling diagram for **NNU-50** was obtained via 3dt (part of the Gavrog package) [45] and shown in Fig. 1(c). Additionally, the contact surface of **NNU-50** is shown in Fig. 1(d), and the potential solvent volume calculated by PLATON [43] software is 31.7%.

In order to evaluate the crystallinity and chemical stability of **NNU-50**, the PXRD experiment was performed on the as-synthesized sample. The PXRD patterns of the synthesized sample match well with the spectrum simulated from the single crystal data, which indicates its high purity and crystallinity. Then, 20 mg of as-synthesized crystals were immersed in 10 mL of 1 M KOH solution for 24 h to evaluate the chemical stability of the sample in robust alkaline solution. The PXRD patterns of the soaked crystals are consistent with the intrinsic PXRD spectrum of the crystalline sample, which demonstrates that **NNU-50** could maintain its structural integrity in 1 M KOH solution (Fig. S8 in the ESM). The structural features of **NNU-50** were further revealed by FTIR spectroscopy (KBr: ν (cm^{-1}) = 2,910 vs, 1,683 s, 1,504 w, 1,477 m, 1,433 s, 1,370 m, 1,341 m, 1,255 w, 1,152 s, 1,086 w, 1,056 s, 799 m, 704 m, 686 m, 657 m, 552 m, 515 m, and 427 m; Fig. S9 in the ESM). Furthermore, the thermal stability of the sample was measured by TGA, and it is found from the TGA curve that the **NNU-50** could maintain structural stability until 280 °C (Fig. S10 in the ESM).

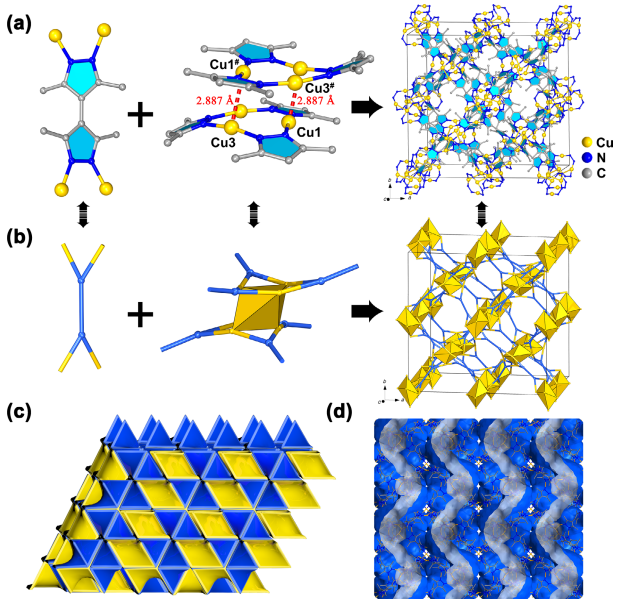

Figure 1 (a) The 3D framework of **NNU-50** constructed by the hexanuclear Cu cluster and Me_4BPz. (b) Simplified diagram of M_4BPz ligand, hexanuclear cluster, and 3D framework. (c) 3D tiling for **NNU-50**. (d) The contact surface for **NNU-50**.

The pore structure of **NNU-50** was verified by gas adsorption tests and the crystals were immersed in methanol for continuously three-day solvent exchange before test. The N_2 adsorption and desorption isotherms at 77 K show a rapidly rising uptake at relative pressure below 0.05, which is a typical microporous adsorption behavior, and the saturation N_2 adsorption capacity is up to 204.89 $cm^3 \cdot g^{-1}$ (Fig. S11 in the ESM). The Brunauer–Emmett–Teller (BET) surface area is 486.46 $m^2 \cdot g^{-1}$ and the total pore volume is 0.30 $cm^3 \cdot g^{-1}$. According to the pore size distribution calculated from the nonlocal density functional theory (NLDFT), the main pore size of **NNU-50** is 0.52 nm, which is consistent with the crystal structure derived from SC-XRD data (Fig. S12 in the ESM). Moreover, the CO_2 adsorption and desorption isotherms were tested under 1 atm to investigate the CO_2 adsorption capacity of **NNU-50** at 273 and 298 K. The results illustrate that the adsorption capacity of **NNU-50** for CO_2 can reach 33.84 and 49.34 $cm^3 \cdot g^{-1}$ at 298 and 273 K, respectively (Fig. S13 in the ESM).

3.2 ECR performance of NNU-50 electrocatalyst

According to its superior chemical stability, the ECR performance of the **NNU-50** was tested in the flow cell equipped with the GDL by using 1 M KOH as electrolyte. To evaluate the electrocatalytic activity of **NNU-50** for the ECR, the LSV curves in the atmosphere of flowing CO_2 and Ar were measured in the range of 0 to −1.3 V vs. RHE, respectively. From Fig. 2(a), it can be found that the onset potential of **NNU-50** in the CO_2 stream is lower than −0.4 V vs. RHE, which implies the possible catalytic activity for ECR of the electrocatalyst. Besides, the current density in the CO_2 atmosphere is much higher than that in Ar, indicating that the **NNU-50** may prefer to support ECR rather than the competitive hydrogen evolution reaction (HER). It is worthy to note that when the reductive potential comes to −1.2 V vs. RHE, the current density in the CO_2 stream is up to 755.86 $mA \cdot cm^{-2}$, which further illustrates the possibly excellent electrocatalytic activity for ECR of the **NNU-50**.

To explore the electrocatalytic selectivity for different reduction products of **NNU-50**, the CO_2 electroreduction experiments were carried out at the selected potential range (−0.6 to −1.2 V vs. RHE). The gaseous products were monitored and quantified in real time by on-line GC. As shown in Fig. 2(b), the CH_4, C_2H_4, CO, and H_2 have been analyzed as the main gaseous products of ECR when it was catalyzed by **NNU-50**. The liquid products were detected by the ^1H NMR, and the result demonstrates that there are almost no liquid products (Fig. S14 in the ESM). Figure 2(b) illustrates that CH_4 is the dominant product from the ECR

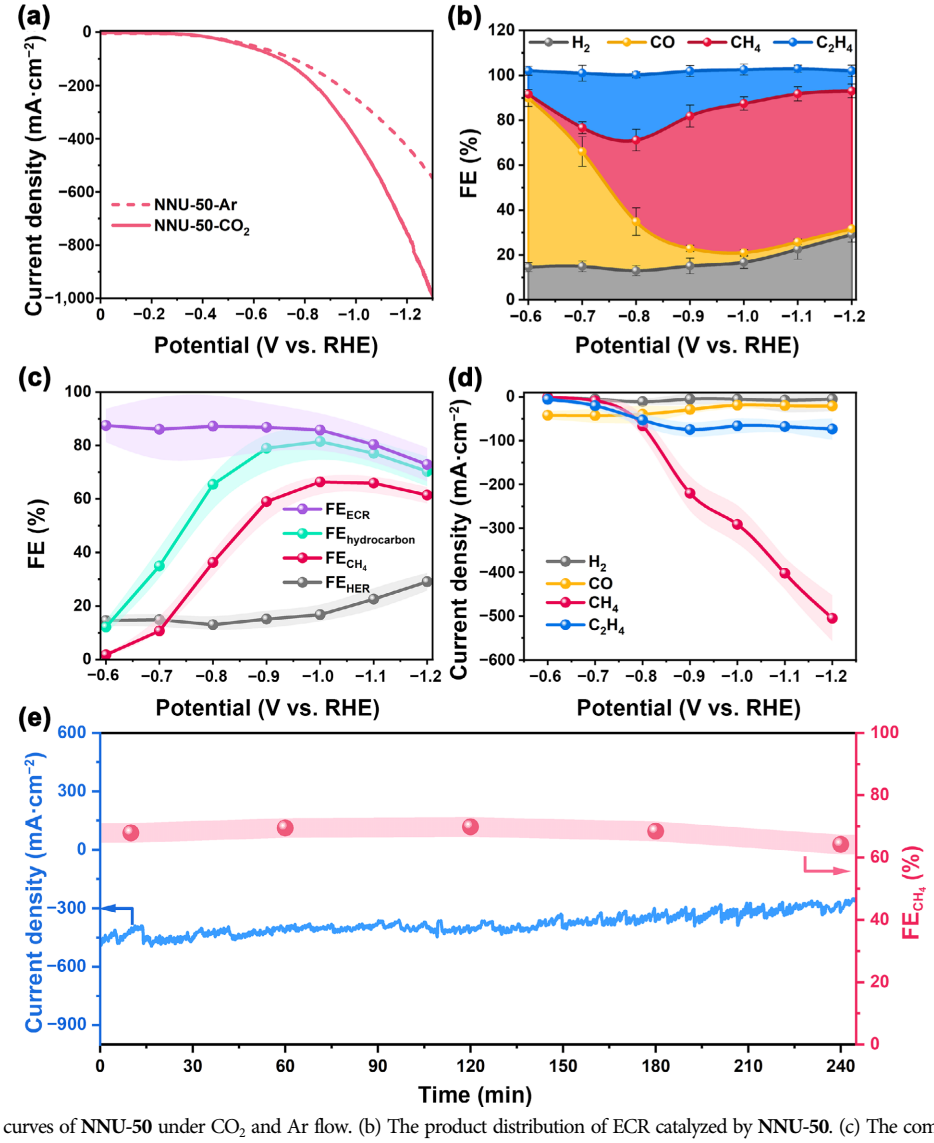

Figure 2 (a) The LSV curves of **NNU-50** under CO_2 and Ar flow. (b) The product distribution of ECR catalyzed by **NNU-50**. (c) The comparison of FEs for ECR, hydrocarbon, CH_4, and HER with **NNU-50** as an electrocatalyst. (d) Partial current densities for different products (H_2, CO, CH_4, and C_2H_4) of **NNU-50**. (e) Chronoamperometric curve of **NNU-50** at −1.0 V vs. RHE during the stability test.

catalyzed by **NNU-50**. Among the gaseous products, the CO and C_2H_4 could compete with CH_4 at relatively low reductive potentials, but with the increase of the potential, the FEs of CO and C_2H_4 decrease gradually and the CH_4 shows an obvious competitive advantage. To be specific, the **NNU-50** gives 75.33% FE_{CO}, 10.43% $FE_{C_2H_4}$, 14.53% FE_{H_2}, and 1.73% FE_{CH_4} at −0.6 V vs. RHE (Table S6 in the ESM). Subsequently, the FE_{CH_4} increases gradually and achieves its peak value of 66.40% when the potential comes to −1.0 V vs. RHE. It is noteworthy that the FE_{CH_4} keeps higher than 58.00% from −0.9 to −1.2 V vs. RHE. Moreover, the FE_{H_2} keeps lower than 17% in the potential range of −0.6 to −1.0 V vs. RHE and only shows a slightly increasing trend after −1.0 V vs. RHE, which signifies the poor selectivity for HER of **NNU-50**. It can be seen from Fig. 2(c) that the total FEs of hydrocarbon could reach up to 81.50% at −1.0 V vs. RHE, suggesting that the **NNU-50** delivers superior selectivity for the electroconversion of CO_2 to high value-added products. It is worth noting that the FE_{ECR} remains at a high level (over 72%) and keeps higher than FE_{HER} at all applied potentials during the whole electrochemical test, which further testifies that **NNU-50** is more inclined to catalyze the ECR than the HER.

To further reveal the electrocatalytic activity of **NNU-50**, the partial current densities of CH_4, C_2H_4, CO, and H_2 have been calculated. As shown in Fig. 2(d), the partial CH_4 current density can reach 505.98 mA·cm^{-2} at −1.2 V vs. RHE, which is much higher than those of other reduction products, illustrating that the **NNU-50** possesses excellent catalytic activity for CH_4.

Considering the important role of catalytic durability in evaluating the practical application potential of electrocatalysts, chronoamperometry experiments were carried out. The short-time stability curves are shown in Fig. S15 in the ESM, reflecting that the ECR catalyzed by **NNU-50** can preserve a stable current at each test potential. The long-term durability of **NNU-50** was assessed by the chronoamperometric curve at −1.0 V vs. RHE, the potential which has achieved the optimal selectivity for CO_2-to-CH_4 conversion (Fig. 2(e)). The current curve was recorded by the electrochemical workstation, and the FE_{CH_4} was monitored with GC every 60 min. The result illustrates that **NNU-50** can maintain the current density of approximately 400 mA·cm^{-2} and FE_{CH_4} over 64.00% during the continuous electrolysis of 240 min. All the aforementioned results demonstrate that the **NNU-50** exhibits superior activity, selectivity, and stability for the electrochemical conversion of CO_2 to CH_4. Notably, the electrocatalytic performance of **NNU-50** is comparable to that of the best-performing MOF electrocatalysts reported up to now (Table S7 in the ESM).

To explore the carbon source of the reduction product, the isotope labeling experiments were performed by using $^{13}CO_2$ instead of $^{12}CO_2$ under the same reaction conditions and the results extracted from GC-MS have been displayed in Fig. S16 in the ESM. It is comprehensible that the signal peaks at m/z = 17, 29, and 30 belong to $^{13}CH_4$, ^{13}CO, and $^{13}C_2H_4$, respectively, which discloses that the carbon-based reduction products indeed originate from the CO_2 used.

To detect reaction intermediates during ECR, the *in situ* DRIFTS tests were performed. As shown in Fig. 3, the peak at 1,443 cm^{-1} can be attributed to the symmetric stretching of HCO_3* [46]. Besides, four new absorption bands appeared at 1,585, 1,409, 1,337, and 1,250 cm^{-1} and strengthened gradually with the irradiation time increasing. These peaks are ascribed to the asymmetric stretching, symmetric stretching, C–O stretching, and OH deformation of the *COOH group, separately, which is usually considered as a key intermediate of electrochemical CO_2-to-CH_4 conversion [47–51]. And the signal of the *CO intermediate was detected at 2,075 cm^{-1}, with a slight blue shift

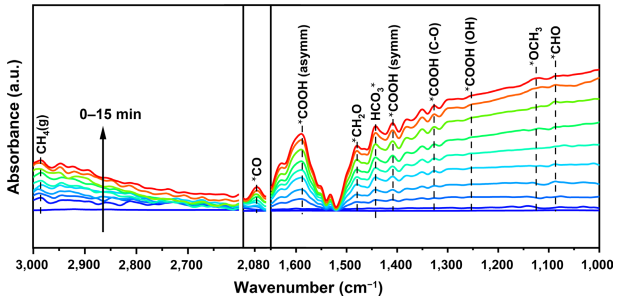

Figure 3 The *in situ* DRIFTS spectra of **NNU-50**.

compared to most reported values (ca. 2,065 cm^{-1}) [18, 22]. Most importantly, the infrared peaks at 1,122, 1,481, and 1,085 cm^{-1} can be assigned to the *CHO, $*CH_2O$, and CH_3O* intermediates, respectively, which are widely accepted as crucial intermediate products of ECR to CH_4 [52, 53]. Based on the analyses of the *in situ* DRIFTS spectra in Fig. 3, the possible reduction pathway of this catalytic system is shown in Table S8 in the ESM.

3.3 The contrast of ECR performance between NNU-50 and Cu_6MePz

For the purpose of further revealing the structural superiority of MOF materials in ECR, the **Cu_6MePz** was synthesized as a contrastive sample. The **Cu_6MePz** is a metal-organic compound constructed by Cu(I) cations and 3,5-dimethylpyrazole (MePz), and its structure has been shown in Fig. S17 in the ESM. Actually, the coordination environment of Cu ions in **Cu_6MePz** is almost identical to **NNU-50**, and the hexanuclear Cu cluster with cuprophilic interactions of **Cu_6MePz** is similar to the SBU of **NNU-50**, thus it can be regarded as a part of **NNU-50** (Fig. S18 in the ESM). The PXRD patterns of crystal sample indicate the high crystallinity and phase purity of as-synthesized **Cu_6MePz** (Fig. S19 in the ESM). Furthermore, the FTIR spectrum of the **Cu_6MePz** sample has been shown in Fig. S20 in the ESM. When **Cu_6MePz** was used as a catalyst for ECR under identical conditions as **NNU-50**, the differences in electrocatalytic performance have been exhibited in Figs. 4(a)–4(c), and Figs. S21–S28 in the ESM. At first, Fig. S21 in the ESM tells that **Cu_6MePz** owns better catalytic activity for ECR than HER. And then the electrocatalytic activity of the two catalysts has been compared, as shown in Fig. 4(a), the **Cu_6MePz** gives a current density of 574.52 mA·cm^{-2} at −1.2 V vs. RHE in the CO_2 atmosphere, which is much lower than that of **NNU-50** (755.86 mA·cm^{-2}), suggesting that its electrocatalysis activity for ECR is probably not as good as the **NNU-50**. Meanwhile, the current densities of two catalysts over various test potentials have been measured and listed in Figs. S15 and S22 in the ESM. It can be found that **NNU-50** exhibits a higher current density than **Cu_6MePz** at each potential, which further implies the better electrocatalytic activity of **NNU-50**. By comparing the structure of **NNU-50** and **Cu_6MePz**, we speculate that the superior activity of **NNU-50** can be attributed to the enhanced electronic conductivity by stronger cuprophilic interactions inside the catalyst structure.

The product distribution in Fig. S23 in the ESM reveals that the CH_4 is also the main product when **Cu_6MePz** is used as an electrocatalyst for ECR. However, the selective conversion of CO_2 to a specific product is not satisfactory enough when the reaction is catalyzed by **Cu_6MePz** for the FE_{CH_4} and $FE_{C_2H_4}$ are comparable during the whole ECR. The contrast of the selectivity for CH_4 between the two electrocatalysts is presented in Fig. 4(b), and it can be concluded that the **NNU-50** performs much better than **Cu_6MePz** for the electrochemical CO_2-to-CH_4 conversion because the FE_{CH_4} of **NNU-50** keeps higher than that of **Cu_6MePz** over a wide potential range (−0.8 to −1.2 V vs. RHE). Besides, as shown

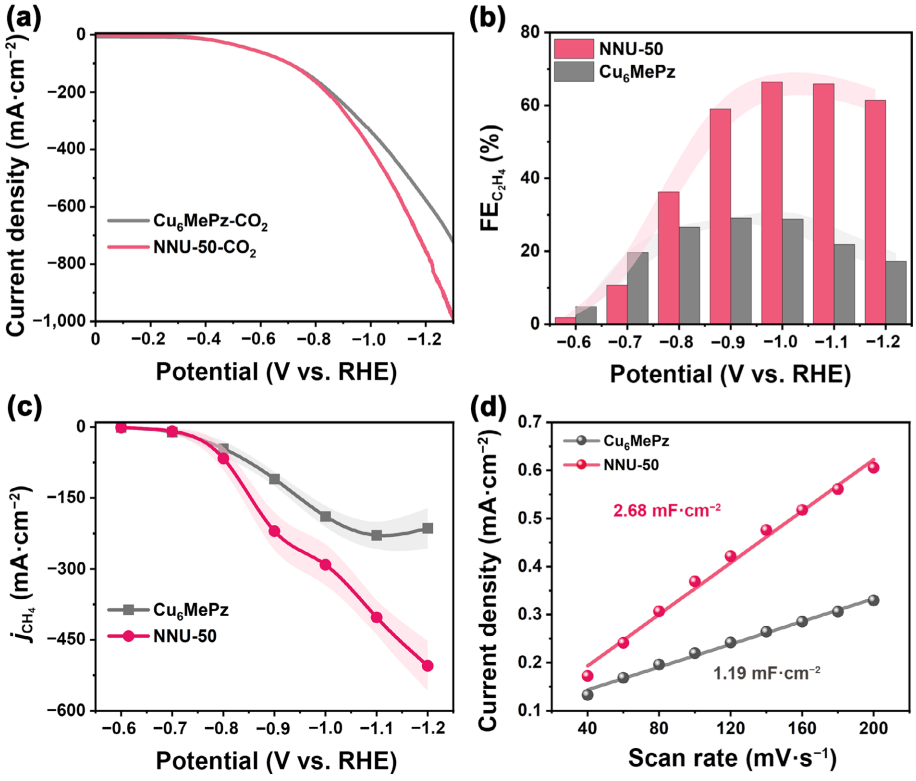

Figure 4 (a) The LSV curves under CO_2, (b) FEs for CH_4, (c) partial current densities for CH_4, and (d) C_{dl} values of NNU-50 and Cu_6MePz.

in Fig. S24 in the ESM, the $FE_{C_2H_4}$ and FE_{CO} of **Cu_6MePz** tend to be higher than those of **NNU-50**, demonstrating the electrocatalytic selectivity for CH_4 of **Cu_6MePz** catalyst is inferior to **NNU-50** from another perspective (Table S9 in the ESM). Interestingly, the FEs of hydrocarbon when ECR is catalyzed by **NNU-50** are higher than those of **Cu_6MePz** over the entire applied potentials (Fig. S25(a) in the ESM), which indicates that the extended porous structure of the MOF materials may facilitate the formation of high value-added products by enriching the substrate and providing more catalytically active sites. Moreover, the FEs for ECR of two catalysts keep at a high level (over 67%) and higher than HER (Fig. S25(b) in the ESM), which proves that both the two catalysts possess excellent selectivity for ECR than competitive reaction (HER). Besides, the blank carbon paper was applied to catalyze ECR to eliminate the effect of the substrate on the electrocatalyst performance. And the results illustrate that the carbon paper shows nearly no electrocatalytic activity for ECR (Fig. S26 in the ESM).

The partial current densities have been calculated to reflect the different activities for various products of **Cu_6MePz**. As displayed in Fig. S27 in the ESM, the partial CH_4 current density of **Cu_6MePz** does not exhibit obviously predominant superiority over the values of other products, indicating that the **Cu_6MePz** delivers unfulfilling activity for the main product. Figure 4(c) shows that the partial current density for CH_4 of **Cu_6MePz** is lower than that of the **NNU-50** from −0.8 to −1.2 V vs. RHE, which means its poorer activity for electrocatalytic CO_2-to-CH_4 conversion. Additionally, the contrasts of partial current densities for C_2H_4 and CO between the two electrocatalysts further reveal the better electrocatalysis activity for CH_4 of **NNU-50** (Fig. S28 in the ESM).

The interesting electrocatalytic performance differences between the **NNU-50** and **Cu_6MePz** attracted us to explore the reasons from the perspective of reaction kinetics. Firstly, the electrochemical double-layer capacitance (C_{dl}) values have been calculated from the CV curves (Fig. S29 in the ESM) to estimate the electrochemical active surface areas (ECSA) of **NNU-50** and **Cu_6MePz**. As shown in Fig. 4(d), the C_{dl} value of **NNU-50** is 2.68 mF·cm^{-2} which is approximately twice larger than that of **Cu_6MePz** (1.19 mF·cm^{-2}), demonstrating that the **NNU-50** possesses more available active sites interacting with electrolyte and thus accelerates the ECR. Furthermore, the electrocatalytic kinetics on the electrode/electrolyte surface in the process of ECR has been investigated by performing the EIS tests of two catalysts at −1.0 V vs. RHE. According to the fitting results of the Nyquist plots (Fig. S30 in the ESM), the **NNU-50** owns much smaller charge transfer resistance than **Cu_6MePz**, which endows it with faster electron transfer efficiency and better electrocatalytic activity for ECR.

3.4 The electrochemical stability characterizations of NNU-50

To further investigate the structural stability of **NNU-50** during the ECR, a series of comparative characterizations have been carried out on the working electrodes. As shown in Fig. 5(a), the PXRD patterns of the electrocatalyst before and after the test are well-matched, demonstrating that the **NNU-50** can maintain its structural integrity in the process of ECR. Significantly, there are no Cu(0), Cu_2O, or CuO signals appearing on the PXRD pattern of **NNU-50** after the electrocatalysis test, which tells that the phase transition does not occur on the electrocatalyst. A similar conclusion can also be drawn by comparing the Raman spectra of sample. From Fig. 5(b), it can be found that the Raman characteristic peaks of Cu_2O (217, 310, 417, 520, 636, and 810 cm^{-1}) or CuO (298, 345, and 632 cm^{-1}) do not appear on the Raman spectra of **NNU-50**, illustrating that **NNU-50** can keep stable when it is used as the catalyst for ECR. This can also be affirmed by comparing ATR-FTIR spectra of the working electrodes coated with the catalyst. As shown in Fig. S31 in the ESM, the ATR-FTIR spectrum of the **NNU-50** catalyst after ECR is consistent with the one before test. Moreover, it could be observed that the morphology of the **NNU-50** catalyst remains basically unchanged before and after electrolysis from the SEM

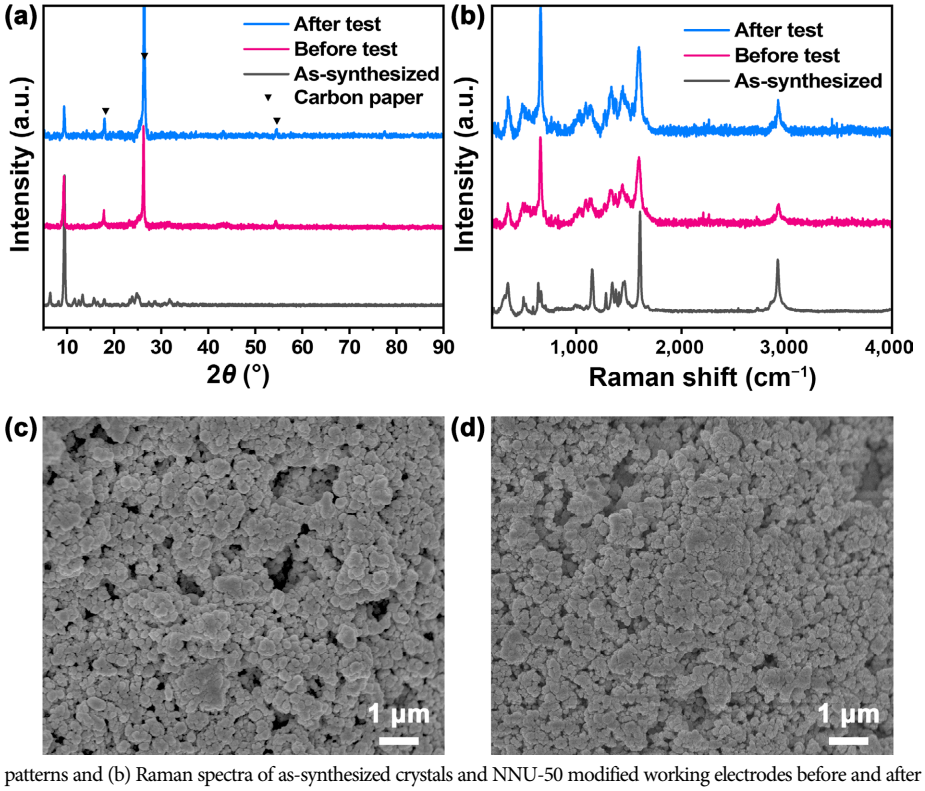

Figure 5 (a) The PXRD patterns and (b) Raman spectra of as-synthesized crystals and NNU-50 modified working electrodes before and after test. The SEM images of NNU-50 catalyst (c) before and (d) after electrochemical ECR.

images of the uniformly ground samples, which further testifies its excellent stability. All the above characterization results indicate the **NNU-50** can indeed be used as a persistent heterogeneous catalyst for ECR.

4 Conclusions

In summary, a stable Cu(I) cluster-based MOF (**NNU-50**) and a Cu(I) metal-organic cluster (**Cu_6MePz**) have been designed and synthesized to be electrocatalysts for the ECR in GDL flow cell. The **Cu_6MePz** possesses a similar host structure to the SBU of **NNU-50** and all the Cu(I) catalytically active sites in the two electrocatalysts are stabilized by strong cuprophilic interactions. When they are used as electrocatalysts for ECR, both **NNU-50** and **Cu_6MePz** exhibit high hydrocarbon selectivity ($FE_{hydrocarbon}$ > 68.50%) at −1.0 V vs. RHE. Interestingly, the **NNU-50** shows a more superior ECR performance than **Cu_6MePz** by delivering a larger ECSA, a higher selectivity for CH_4 (66.40%), hydrocarbon (81.50%), and a much larger current density (~ 400 mA·cm^{-2}) at −1.0 V vs. RHE, which can be attributed to the stronger CO_2 adsorption capacity and cuprophilic interactions in **NNU-50**. Significantly, it represents one of the best-performing stable MOF catalysts for efficient electroreduction of CO_2 to CH_4 so far. This is the first case to use Cu(I)-based MOF with cuprophilic interactions as catalysts for ECR, which opens up a broad horizon for the design of efficient Cu-based MOF electrocatalysts.

Acknowledgements

This work was financially supported by the National Natural Science Foundation of China (Nos. 21871141, 21871142, 22071109, 22105080, and 92061101), the Excellent Youth Foundation of Jiangsu Natural Science Foundation (No. BK20211593), Priority Academic Program Development of Jiangsu Higher Education Institutions, and the Foundation of Jiangsu Collaborative Innovation Center of Biomedical Functional Materials.

Electronic Supplementary Material: Supplementary material (further details of electrochemical performance and FTIR spectroscopy measurements and so on) is available in the online version of this article at https://doi.org/10.1007/s12274-022-4681-z.

References

[1] van Soest, H. L.; den Elzen, M. G. J.; van Vuuren, D. P. Net-zero emission targets for major emitting countries consistent with the Paris Agreement. *Nat. Commun.* **2021**, *12*, 2140.

[2] Wang, L. M.; Chen, W. L.; Zhang, D. D.; Du, Y. P.; Amal, R.; Qiao, S. Z.; Wu, J. B.; Yin, Z. Y. Surface strategies for catalytic CO_2 reduction: From two-dimensional materials to nanoclusters to single atoms. *Chem. Soc. Rev.* **2019**, *48*, 5310–5349.

[3] Long, C.; Li, X.; Guo, J.; Shi, Y. N.; Liu, S. Q.; Tang, Z. Y. Electrochemical reduction of CO_2 over heterogeneous catalysts in aqueous solution: Recent progress and perspectives. *Small Methods* **2019**, *3*, 1800369.

[4] Birdja, Y. Y.; Pérez-Gallent, E.; Figueiredo, M. C.; Göttle, A. J.; Calle-Vallejo, F.; Koper, M. T. M. Advances and challenges in understanding the electrocatalytic conversion of carbon dioxide to fuels. *Nat. Energy* **2019**, *4*, 732–745.

[5] Li, L.; Li, X. D.; Sun, Y. F.; Xie, Y. Rational design of electrocatalytic carbon dioxide reduction for a zero-carbon network. *Chem. Soc. Rev.* **2022**, *51*, 1234–1252.

[6] Liu, X. J.; Yang, H.; He, J.; Liu, H. X.; Song, L. D.; Li, L.; Luo, J. Highly active, durable ultrathin $MoTe_2$ layers for the electroreduction of CO_2 to CH_4. *Small* **2018**, *14*, 1704049.

[7] Zhu, D. D.; Liu, J. L.; Qiao, S. Z. Recent advances in inorganic heterogeneous electrocatalysts for reduction of carbon dioxide. *Adv. Mater.* **2016**, *28*, 3423–3452.

[8] Liang, Z. Z.; Wang, H. Y.; Zheng, H. Q.; Zhang, W.; Cao, R. Porphyrin-based frameworks for oxygen electrocatalysis and catalytic reduction of carbon dioxide. *Chem. Soc. Rev.* **2021**, *50*, 2540–2581.

[9] Wang, G. X.; Chen, J. X.; Ding, Y. C.; Cai, P. W.; Yi, L. C.; Li, Y.; Tu, C. Y.; Hou, Y.; Wen, Z. H.; Dai, L. M. Electrocatalysis for CO_2 conversion: From fundamentals to value-added products. *Chem. Soc. Rev.* **2021**, *50*, 4993–5061.

[10] Jung, H.; Lee, S. Y.; Lee, C. W.; Cho, M. K.; Won, D. H.; Kim, C.; Oh, H. S.; Min, B. K.; Hwang, Y. J. Electrochemical fragmentation of Cu_2O nanoparticles enhancing selective C–C coupling from CO_2 reduction reaction. *J. Am. Chem. Soc.* **2019**, *141*, 4624–4633.
[11] Kim, J.; Choi, W.; Park, J. W.; Kim, C.; Kim, M.; Song, H. Branched copper oxide nanoparticles induce highly selective ethylene production by electrochemical carbon dioxide reduction. *J. Am. Chem. Soc.* **2019**, *141*, 6986–6994.
[12] Reske, R.; Mistry, H.; Behafarid, F.; Roldan Cuenya, B.; Strasser, P. Particle size effects in the catalytic electroreduction of CO_2 on Cu nanoparticles. *J. Am. Chem. Soc.* **2014**, *136*, 6978–6986.
[13] Kim, D.; Kley, C. S.; Li, Y. F.; Yang, P. D. Copper nanoparticle ensembles for selective electroreduction of CO_2 to C_2-C_3 products. *Proc. Natl. Acad. Sci. USA* **2017**, *114*, 10560–10565.
[14] Weng, Z.; Jiang, J. B.; Wu, Y. S.; Wu, Z. S.; Guo, X. T.; Materna, K. L.; Liu, W.; Batista, V. S.; Brudvig, G. W.; Wang, H. L. Electrochemical CO_2 reduction to hydrocarbons on a heterogeneous molecular Cu catalyst in aqueous solution. *J. Am. Chem. Soc.* **2016**, *138*, 8076–8079.
[15] Lu, Y. F.; Dong, L. Z.; Liu, J.; Yang, R. X.; Liu, J. J.; Zhang, Y.; Zhang, L.; Wang, Y. R.; Li, S. L.; Lan, Y. Q. Predesign of catalytically active sites via stable coordination cluster model system for electroreduction of CO_2 to ethylene. *Angew. Chem., Int. Ed.* **2021**, *60*, 26210–26217.
[16] Wang, R.; Liu, J.; Huang, Q.; Dong, L. Z.; Li, S. L.; Lan, Y. Q. Partial coordination-perturbed Bi-copper sites for selective electroreduction of CO_2 to hydrocarbons. *Angew. Chem., Int. Ed.* **2021**, *60*, 19829–19835.
[17] Wang, Y. R.; Liu, M.; Gao, G. K.; Yang, Y. L.; Yang, R. X.; Ding, H. M.; Chen, Y. F.; Li, S. L.; Lan, Y. Q. Implanting numerous hydrogen-bonding networks in a Cu-porphyrin-based nanosheet to boost CH_4 selectivity in neutral-media CO_2 electroreduction. *Angew. Chem., Int. Ed.* **2021**, *60*, 21952–21958.
[18] Wang, Y. R.; Ding, H. M.; Ma, X. Y.; Liu, M.; Yang, Y. L.; Chen, Y. F.; Li, S. L.; Lan, Y. Q. Imparting CO_2 electroreduction auxiliary for integrated morphology tuning and performance boosting in a porphyrin-based covalent organic framework. *Angew. Chem., Int. Ed.* **2022**, *61*, e202114648.
[19] Bushuyev, O. S.; De Luna, P.; Cao Thang, D.; Tao, L.; Saur, G.; van de lagemaat, J.; Kelley, S. O.; Sargent, E. H. What should we make with CO_2 and how can we make it? *Joule* **2018**, *2*, 825–832.
[20] Liu, J. J.; Song, X. Y.; Zhang, T.; Liu, S. Y.; Wen, H. R.; Chen, L. 2D conductive metal-organic frameworks: An emerging platform for electrochemical energy storage. *Angew. Chem., Int. Ed.* **2021**, *60*, 5612–5624.
[21] Chen, S. H.; Su, Y. Q.; Deng, P. L.; Qi, R. J.; Zhu, J. X.; Chen, J. X.; Wang, Z. T.; Zhou, L.; Guo, X. P.; Xia, B. Y. Highly selective carbon dioxide electroreduction on structure-evolved copper perovskite oxide toward methane production. *ACS Catal.* **2020**, *10*, 4640–4646.
[22] Yi, J. D.; Xie, R. K.; Xie, Z. L.; Chai, G. L.; Liu, T. F.; Chen, R. P.; Huang, Y. B.; Cao, R. Highly selective CO_2 electroreduction to CH_4 by *in situ* generated Cu_2O single-type sites on a conductive MOF: Stabilizing key intermediates with hydrogen bonding. *Angew. Chem., Int. Ed.* **2020**, *59*, 23641–23648.
[23] Zhu, H. L.; Huang, J. R.; Zhang, X. W.; Wang, C.; Huang, N. Y.; Liao, P. Q.; Chen, X. M. Highly efficient electroconversion of CO_2 into CH_4 by a metal-organic framework with trigonal pyramidal $Cu(I)N_3$ active sites. *ACS Catal.* **2021**, *11*, 11786–11792.
[24] Zhuo, L. L.; Chen, P.; Zheng, K.; Zhang, X. W.; Wu, J. X.; Lin, D. Y.; Liu, S. Y.; Wang, Z. S.; Liu, J. Y.; Zhou, D. D. et al. Flexible cuprous triazolate frameworks as highly stable and efficient electrocatalysts for CO_2 reduction with tunable C_2H_4/CH_4 selectivity. *Angew. Chem., Int. Ed.*, in press, https://doi.org/10.1002/anie.202204967.
[25] Zhang, L.; Li, X. X.; Lang, Z. L.; Liu, Y.; Liu, J.; Yuan, L.; Lu, W. Y.; Xia, Y. S.; Dong, L. Z.; Yuan, D. Q. et al. Enhanced cuprophilic interactions in crystalline catalysts facilitate the highly selective electroreduction of CO_2 to CH_4. *J. Am. Chem. Soc.* **2021**, *143*, 3808–3816.
[26] Harisomayajula, N. V. S.; Makovetskyi, S.; Tsai, Y. C. Cuprophilic Interactions in and between Molecular Entities. *Chem.—Eur. J.* **2019**, *25*, 8936–8954.
[27] Furukawa, H.; Cordova, K. E.; O'Keeffe, M.; Yaghi, O. M. The chemistry and applications of metal-organic frameworks. *Science* **2013**, *341*, 1230444.
[28] Zhou, J. W.; Li, R.; Fan, X. X.; Chen, Y. F.; Han, R. D.; Li, W.; Zheng, J.; Wang, B.; Li, X. G. Rational design of a metal-organic framework host for sulfur storage in fast, long-cycle Li-S batteries. *Energy Environ. Sci.* **2014**, *7*, 2715–2724.
[29] Qiu, Y. L.; Zhong, H. X.; Zhang, T. T.; Xu, W. B.; Su, P. P.; Li, X. F.; Zhang, H. M. Selective electrochemical reduction of carbon dioxide using Cu based metal organic framework for CO_2 capture. *ACS Appl. Mater. Interfaces* **2018**, *10*, 2480–2489.
[30] Zhang, Y.; Dong, L. Z.; Li, S.; Huang, X.; Chang, J. N.; Wang, J. H.; Zhou, J.; Li, S. L.; Lan, Y. Q. Coordination environment dependent selectivity of single-site-Cu enriched crystalline porous catalysts in CO_2 reduction to CH_4. *Nat. Commun.* **2021**, *12*, 6390.
[31] Nam, D. H.; Bushuyev, O. S.; Li, J.; De Luna, P.; Seifitokaldani, A.; Dinh, C. T.; García de Arquer, F. P.; Wang, Y. H.; Liang, Z. Q.; Proppe, A. H. et al. Metal-organic frameworks mediate Cu coordination for selective CO_2 electroreduction. *J. Am. Chem. Soc.* **2018**, *140*, 11378–11386.
[32] Qiu, X. F.; Zhu, H. L.; Huang, J. R.; Liao, P. Q.; Chen, X. M. Highly selective CO_2 electroreduction to C_2H_4 using a metal-organic framework with dual active sites. *J. Am. Chem. Soc.* **2021**, *143*, 7242–7246.
[33] Yang, F.; Chen, A. L.; Deng, P. L.; Zhou, Y. Z.; Shahid, Z.; Liu, H. F.; Xia, B. Y. Highly efficient electroconversion of carbon dioxide into hydrocarbons by cathodized copper-organic frameworks. *Chem. Sci.* **2019**, *10*, 7975–7981.
[34] Liu, Y. Z.; Li, S.; Dai, L.; Li, J. N.; Lv, J. N.; Zhu, Z. J. J.; Yin, A. X.; Li, P. F.; Wang, B. The synthesis of Hexaazatrinaphthylene-based 2D conjugated copper metal-organic framework for highly selective and stable electroreduction of CO_2 to methane. *Angew. Chem., Int. Ed.* **2021**, *60*, 16409–16415.
[35] Liu, Y. Y.; Zhu, H. L.; Zhao, Z. H.; Huang, N. Y.; Liao, P. Q.; Chen, X. M. Insight into the effect of the d-orbital energy of copper ions in metal-organic frameworks on the selectivity of electroreduction of CO_2 to CH_4. *ACS Catal.* **2022**, *12*, 2749–2755.
[36] Almeida, Q. A. R. Synthesis of highly substituted pyrroles using ultrasound in aqueous media. *Green Chem. Lett. Rev.* **2013**, *6*, 129–133.
[37] Boldog, I.; Rusanov, E. B.; Chernega, A. N.; Sieler, J.; Domasevitch, K. V. One- and two-dimensional coordination polymers of 3,3′,5,5′-tetramethyl-4,4′-bipyrazolyl, a new perspective crystal engineering module. *Polyhedron* **2001**, *20*, 887–897.
[38] He, J.; Yin, Y. G.; Wu, T.; Li, D.; Huang, X. C. Design and solvothermal synthesis of luminescent copper(I)-pyrazolate coordination oligomer and polymer frameworks. *Chem. Commun.* **2006**, *27*, 2845–2847.
[39] Bruker Inc. *APEX2, SAINT and SADABS*; Bruker AXS: Madison, USA, 2009.
[40] Sheldrick, G. M. *SHELXT*—Integrated space-group and crystal-structure determination. *Acta Cryst.* **2015**, *A71*, 3–8.
[41] Sheldrick, G. M. Crystal structure refinement with *SHELXL*. *Acta Cryst.* **2015**, *C71*, 3–8.
[42] Dolomanov, O. V.; Bourhis, L. J.; Gildea, R. J.; Howard, J. A. K.; Puschmann, H. OLEX2:A complete structure solution, refinement and analysis program. J. Appl. *Cryst.* **2009**, *42*, 339–341.
[43] Spek, A. L. PLATON SQUEEZE: A tool for the calculation of the disordered solvent contribution to the calculated structure factors. *Acta Cryst.* **2015**, *C71*, 9–18.
[44] Blatov, V. A.; Shevchenko, A. P.; Proserpio, D. M. Applied topological analysis of crystal structures with the program package ToposPro. *Cryst. Growth Des.* **2014**, *14*, 3576–3586.
[45] Delgado-Friedrichs, O. *The GAVROG Project* [Online]. http://www.gavrog.org/ (accessed Mar 10, 2022).
[46] Wu, J. C. S.; Huang, C. W. *In situ* DRIFTS study of photocatalytic CO_2 reduction under UV irradiation. *Front. Chem. Eng. China* **2010**,

4, 120–126.

[47] Li, X. D.; Sun, Y. F.; Xu, J. Q.; Shao, Y. J.; Wu, J.; Xu, X. L.; Pan, Y.; Ju, H. X.; Zhu, J. F.; Xie, Y. Selective visible-light-driven photocatalytic CO_2 reduction to CH_4 mediated by atomically thin $CuIn_5S_8$ layers. *Nat. Energy* **2019**, *4*, 690–699.

[48] Zhu, S. Q.; Li, T. H.; Cai, W. B.; Shao, M. H. CO_2 electrochemical reduction As probed through infrared spectroscopy. *ACS Energy Lett.* **2019**, *4*, 682–689.

[49] Firet, N. J.; Smith, W. A. Probing the reaction mechanism of CO_2 electroreduction over Ag films via operando infrared spectroscopy. *ACS Catal.* **2017**, *7*, 606–612.

[50] Pérez-Gallent, E.; Figueiredo, M. C.; Calle-Vallejo, F.; Koper, M. T. M. Spectroscopic observation of a hydrogenated CO dimer intermediate during CO reduction on Cu (100) electrodes. *Angew. Chem., Int. Ed.* **2017**, *56*, 3621–3624.

[51] Stevens, R. W.; Chuang, S. S. C. *In situ* IR study of transient CO_2 reforming of CH_4 over Rh/Al_2O_3. *J. Phys. Chem. B* **2004**, *108*, 696–703.

[52] Liu, Y. M.; Chen, S.; Quan, X.; Yu, H. T. Efficient electrochemical reduction of carbon dioxide to acetate on nitrogen-doped nanodiamond. *J. Am. Chem. Soc.* **2015**, *137*, 11631–11636.

[53] Ewing, G. E.; Thompson, W. E.; Pimentel, G. C. Infrared detection of the formyl radical HCO. *J. Chem. Phys.* **1960**, *32*, 927–932.